Journal of Colloid and Interface Science 571 (2020) 419–428

Contents lists available at ScienceDirect

Journal of Colloid and Interface Science

journal homepage: www.elsevier.com/locate/jcis

Scattering from colloidal cubic silica shells: Part I, particle form factors and optical contrast variation

F. Dekker [a], B.W.M. Kuipers [a], A.V. Petukhov [a,b], R. Tuinier [a,b], A.P. Philipse [a,*]

[a] Van't Hoff Laboratory for Physical and Colloid Chemistry, Debye Institute for Nanomaterials Science, Padulaan 8, 3584 CH, Utrecht University, the Netherlands
[b] Laboratory of Physical Chemistry, Department of Chemical Engineering and Chemistry & Institute for Complex Molecular Systems, Eindhoven University of Technology, P.O. Box 513, 5600 MB Eindhoven, the Netherlands

HIGHLIGHTS

- In-depth scattering study on dilute dispersions of cubic silica shells (CSS).
- Small angle X-ray scattering manifests a shape intermediate a spherical and cubic shell.
- Static light scattering demonstrates the cubic CSS form stable dispersions.
- CSS are optically homogeneous with and refractive index independent of thickness.

GRAPHICAL ABSTRACT

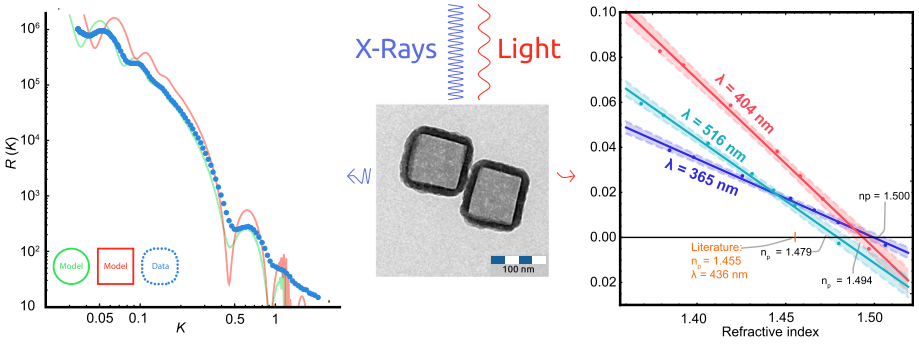

ARTICLE INFO

Article history:
Received 1 August 2019
Revised 31 October 2019
Accepted 1 November 2019
Available online 20 November 2019

Keywords:
Static light scattering
Small angle X-ray scattering
Contrast variation
Colloidal cubic shells
Colloidal core-shell particles
Particle form factor
Guinier approximation

ABSTRACT

Hypothesis: Colloidal cubic silica shells, prepared from cuprous oxide cubes, with a typical size of 100 nm are promising model particles for scattering studies on dilute, as well as concentrated fluids, of non-spherical colloids.

Experiments: Small angle X-ray scattering, and static light scattering are employed to determine form factors of cubic silica shells and silica covered cuprous oxide cubes. Contrast variation experiments are performed to assess the refractive index and optical homogeneity of the cubic silica shells, which is important for the extension of the scattering study to concentrated dispersions of cubic shells in Part II (Dekker, submitted for publication).

Results: The experimental form factors, which compare well to theoretical form factors, manifest cubic silica shells that are dispersed as single stable colloids with a shape intermediate between a sphere and a perfect cube. Contrast variation demonstrates that the silica shells are optically homogeneous, with a refractive index that is independent of the shell thickness. The results presented here open up the possibility to extract structure factors from light scattering measurements on concentrated cube dispersions in Part II.

1. Introduction

The thermodynamic properties of cube fluids, such as the equation of state, have not yet been measured experimentally. Current insight is based upon only a few theoretical [1] and simulation [2,3] studies. In part II of this research [4] we present the

* Corresponding author.
E-mail address: A.P.Philipse@uu.nl (A.P. Philipse).

https://doi.org/10.1016/j.jcis.2019.11.002
0021-9797/

experimental equation of state and static structure factors of colloidal cubic silica shells (CSS), determined from static light scattering (SLS) data. In order to study stable dispersion of colloidal cubes with SLS, particles with a size in the range of 100–200 nm are desired. Recently we developed a preparation method for CSS with average sizes between 100 and 150 nm [5]. These shells are expected to be suitable model particles to study the thermodynamic properties of concentrated cube fluids.

In literature, colloids with a rounded cubic shape are often described as superballs with a specific shape parameter m. Superballs are a mathematical shape described by [6]:

$$\left|2\frac{x}{R_{el}}\right|^m + \left|2\frac{y}{R_{el}}\right|^m + \left|2\frac{z}{R_{el}}\right|^m = 1 \quad (1)$$

where R_{el} is the edge length of the superball. For $m = 2$ and $m = \infty$, Eq. (1) describes a perfect sphere and a perfect cube, respectively. For intermediate m values, Eq. (1) describes a rounded cube. Scattering measurements on concentrated dispersions of cubes, requires knowledge of single particles properties, such as the internal refractive index profile, details on the particle shape, and their corresponding form factor. The complex shape of the cubic silica shells makes it difficult to calculate these properties *ab initio*, so one has to rely on experiments. Therefore, the goal of this paper is to characterise the scattering properties of dilute dispersions of CSS in detail.

Nowadays, well defined colloidal cubes can be prepared in different sizes and in various materials [7–13]. These cubic particles are of interest since they form different crystal structures compared to spherical particles [14–16]. Understanding how cubic particles respond to shear [17,18] and assemble in confinement [19,20,15,21] or on interfaces [22,23] is therefore a current topic of research, in light of the envisioned applications of cubic colloids in sensing [24], catalysis [8] and energy storage [25].

Cubic silica shells with sizes ranging between 100 and 150 nm are promising for applications in thin film optical coatings [26]. The thickness and refractive index profile dictate the properties and performance of these optical coatings [27]. Optical coatings are often used to decrease reflection [28], and on glass surfaces are often prepared from porous materials [29]. Using anisotropic particles to produce optical coatings is limited to needle shaped particles [30] and little is known on the properties of coatings prepared from cubic colloids. Detailed characterisation of cubic silica shells is required to evaluate the applicability of silica shells in optical films.

Scattering techniques such as SLS and dynamic light scattering (DLS), small angle X-ray scattering (SAXS) and small angle neutron scattering (SANS) are often employed to characterise particulate colloids [31]. SLS for instance, allows for detailed characterisation of the size and optical properties of particles [32,33], as well as probing the interactions and structure of the dispersion [34]. Most experiments and theory regarding SLS on colloids focused on spheres [35,36], although the scattering of anisotropic particles like rod [37] and disk-like [38] particles are also well understood [39,40]. Silver bromide cubes have been studied with SLS [41], and also multiple reports of SAXS and SANS on dilute [14,42–44] and concentrated [45,46,14] dispersions of cubic particles have been reported. Scattering on stable dispersions of cubic shells is, to the best of our knowledge, still lacking. Combining light and X-ray scattering allows for a detailed characterisation of submicron particles because the wave vector (K) range in both techniques complement each other (typically for SLS $K \leqslant 0.05\,\mathrm{nm}^{-1}$ and SAXS $K \geqslant 0.05\,\mathrm{nm}^{-1}$).

In this paper we first report measurements of hollow particle form factors with both SLS and SAXS. These experimental form factors are subsequently compared to theoretical form factors of polydisperse cubic particles and polydisperse spherical particles and results from transmission electron microscopy. Finally, we report a contrast variation study to probe the refractive index profile of the silica shells.

2. Theory: static light scattering

SLS yields the angular scattering intensity profile $I(K)$ of an ensemble of particles as a function of scattering wave vector K, defined as:

$$K = \frac{4\pi n_m}{\lambda_0}\sin\frac{\theta}{2}. \quad (2)$$

Here λ_0 is the wavelength of light in vacuum, n_m is the refractive index of the solution and θ is the scattering angle with respect to the incident beam. In a typical scattering experiment, the intensity of the scattered light is measured at different scattering angles, yielding a $I(\theta)$ or $I(K)$ profile. In the Rayleigh-Gans-Debye approximation, the normalized excess scattering intensity from particles over the that of the solvent is given by the Rayleigh ratio $R(K)$. For sufficiently dilute dispersions, $R(K)$ can, for vertically polarized light, be written as [36,33]:

$$R(K) = P(K)\,v_c^2\rho(n_c - n_s)^2 2\pi^2 n_m^2 \lambda_0^{-4}. \quad (3)$$

Here, $P(K)$ is the form factor, v_c is the volume of the particle, ρ is the particle number density, and n_c, n_s, and n_m are the refractive index of the particle, solvent and dispersion, respectively. The form factor reflects the internal structure of the particle, which is defined as [32]:

$$P(K) = \frac{\left\langle |F(K)|^2 \right\rangle}{\left\langle |F(0)|^2 \right\rangle}. \quad (4)$$

Here $F(K)$ is the particle scattering amplitude of the particle:

$$F(\vec{K}) = \int_v (n_c(\vec{r}) - n_s)e^{i\vec{K}\cdot\vec{r}}\,dV \quad (5)$$

and is obtained by integrating over all scattered waves ($e^{i\vec{K}\cdot\vec{r}}$) within the particle. In Eq. (5) $n_c(\vec{r})$ is the local refractive index of the particle at position $r\rightarrow$ inside the particle. An analytical expression of $P(K)$ is available for several particle shapes, such as thin rods and spherically symmetric particles [40]. For a cubic shell with a homogeneous refractive index profile, the form factor amplitude $F(K)$ is given by [40,47]:

$$F(\vec{K}) = \frac{\left(\frac{V_c(R_1)\sin(K_xR_1)\sin(K_yR_1)\sin(K_zR_1)}{K_xK_yK_zR_1^3} - \frac{V_c(R_2)\sin(K_xR_2)\sin(K_yR_2)\sin(K_zR_2)}{K_xK_yK_zR_2^3}\right)}{(V_c(R_1) - V_c(R_2))}. \quad (6)$$

Here R_1 and R_2 are, respectively, halve of the edge-length of the outer cube and the inner void, and $K_{x,y,z}$ are projections of the scattering vectors on the corresponding axes depicted in Fig. A.1 (in the supplementary information), and $V_c(R_i)$ is the volume of cube with edge-length R_i. To obtain the form factor, the modulus square of Eq. (6) should be orientationally averaged, which can be performed numerically (Eq. A.15 in the supplementary information). Without numerical fitting of the data, however, some important particle properties can already be obtained from the scattering profiles $R(K)$ in the small K regime where the Guinier approximation holds [35]:

$$P(K) = \exp\left(-\frac{K^2R_g^2}{3}\right). \quad (7)$$

Determining the slope from the form factor by:

$$\frac{d\ln(P(K))}{dK^2} = -\frac{R_g^2}{3} \tag{8}$$

yields R_g, the radius of gyration of the particles, a measure of the scattering contrast distribution around the particles centre of mass. For optically homogeneous particles, R_g is defined as:

$$R_g^2 = \frac{\int_v R^2 dV}{\int_v dV} \tag{9}$$

where R is the distance from the centre of mass of the particle. In the SI (Appendix C) it is shown that for a solid cube and a cubic shell, the radii of gyration are respectively given by [48]:

$$R_g = R \tag{10}$$

and

$$R_g^2 = \frac{R_1^5 - R_2^5}{R_1^3 - R_2^3}. \tag{11}$$

In addition to the radius of gyration, the average refractive index of the particles and optical inhomogeneities can be obtained from SLS [33,49]. Following Philipse et al. [49], we write for an optically inhomogeneous particle the refractive index profile $n_c(r)$ of the particle as the average refractive index plus the local deviation $\Delta n_c(r)$:

$$n_c(r) = n_c + \Delta n_c(r). \tag{12}$$

One can then split Eq. (5) into two parts:

$$F(K) = F_0(K) + \epsilon(K) \tag{13}$$

where $F_0(K)$ is the scattering amplitude for a cubic shell with homogeneous refractive index n_c and the form factor amplitude $F(K)$ defined by Eq. (5). The term $\epsilon(K)$ arises from the inhomogeneities in the refractive index ($\Delta n_c(r)$) and can be written as:

$$\epsilon(K) = \int_v \Delta n(r) e^{i\vec{K}\cdot\vec{r}} dV. \tag{14}$$

In the limit $K \to 0$ only the average particle refractive index contributes to the zero angle scattering since $\epsilon(K)$ reduces to zero [49]. To obtain the particle refractive index Eq. (3) should be rewritten to:

$$\frac{1}{n_m}\left[\frac{R(K)}{c}\right]^{1/2} = (n_c - n_s)\, v_c P(K)^{1/2} (Q^*)^{1/2} \tag{15}$$

with:

$$Q^* = \frac{2\pi^2\delta}{\lambda_0^4}. \tag{16}$$

where δ is the number of particles per unit mass (kg^{-1}) and c is the particle concentration in $kg\,m^{-3}$. Eq. (15) implies that when the scattering intensity vanishes, the particles are perfectly index matched, and the refractive index of the particles is equal to the refractive index of the solvent. At scattering wave vectors $K \neq 0$, heterogeneities in the refractive index profile of the particle (Eq. (14)) contribute to the total scattering intensity. These heterogeneities will result in different apparent refractive indices at different K values [49]. Determining the changes in apparent refractive index at different angles will assess the homogeneity of the silica shells.

3. Materials and methods

3.1. Materials

Dimethyl sulfoxide (99.7%) and toluene (99,8+%, p.a. grade) were purchased from Acrös Organics. N,-N,dimethylformamide (anhydrous, 99.8%) was acquired from Sigma-Aldrich and ethanol (technical grade) was obtained from Interchema.

Table 1
Overview of the prepared particles and results of size and shape from TEM

Code	Core size R_2 (nm)	Size R_1 (nm)	Shell thickness (nm)	m value
CSS1	87.9 ± 9	112 ± 10	12	4.5
CSS2	87.9 ± 9	104 ± 9	5	4.3
CSS3	87.9 ± 9	118 ± 12	15	4.0
CSS4	121 ± 20	150 ± 20	15	4.0
CSS5	103 ± 10	128 ± 11	13	3.7
CCS	112 ± 11	133 ± 10	10	4.5

3.2. Preparation of cubic silica shells (CSS)

Cubic silica shells (CSS) were prepared by using a template of cubic Cu_2O nanoparticles. The Cu_2O particles were coated with a silica shell using the PVP-assisted Stöber method [50,51] to obtain cubic core shell particles (CCS). cubic silica shells (CSS) were then obtained by dissolving the core in nitric acid. Experimental details are reported in [5]. The dimensions of the particles used in this research are listed in Table 1. Transmission electron microscope samples were prepared by adding a drop of particle dispersion to 0.5 mL water. A single drop of this diluted dispersion was then deposited on a carbon coated copper grid and dried under a heating lamp for 1 h. Micrographs are presented in Fig. 1.

3.3. Static light scattering

For the analysis of particles with static light scattering (SLS), a homebuilt setup was used. A schematic overview of the setup is depicted in Fig. D.2 in the SI. In the setup a mercury lamp is used as a light source. The light passes several optical filters to control the intensity, wavelength, polarisation and beam width/height. The scattered light is collected by a rotating detector that scans between an angle of 20° and 140°. The sample is prepared by redispersing the particles in solvents filtered with 0.2 µm PTFE filters and transferring the dispersion to a dust-free cuvette. The cuvette is then placed in a toluene bath to perform the experiment (see Table 3).

3.4. Contrast variation measurements

Particles were redispersed from ethanol in DMSO by washing through centrifugation as follows the particles were centrifuged for 15 min at 16,000 g, the supernatant was removed and the particles were redispersed in filtered DMSO by sonication and vortexing. These washing steps were done at least five times to ensure no ethanol was present in the dispersion. The particles in DMSO were then added to mixtures with known concentration of ethanol and DMSO as listed in Table D.1 in the SI. SLS samples were then prepared according to 3.3 The refractive index of these mixtures were calculated with the Bruggeman mixing formula for two components [52]:

$$\chi_1 \frac{n_1^2 - n_{eff}^2}{n_1^2 + 2n_{eff}^2} + (1 - \chi_1)\frac{n_2^2 - n_{eff}^2}{n_2^2 + 2n_{eff}^2} = 0 \tag{17}$$

where χ_1 is the mole fraction of component one, n_1, n_2 and n_{eff} are the refractive indices of components one, two and the effective refractive index of the mixture, respectively. To check whether this formula holds for the used ethanol/DMSO mixtures, calculated values were compared to values obtained with an Abbe refractometer. It was found that for all ethanol/DMSO mixtures in Table D.1 in the

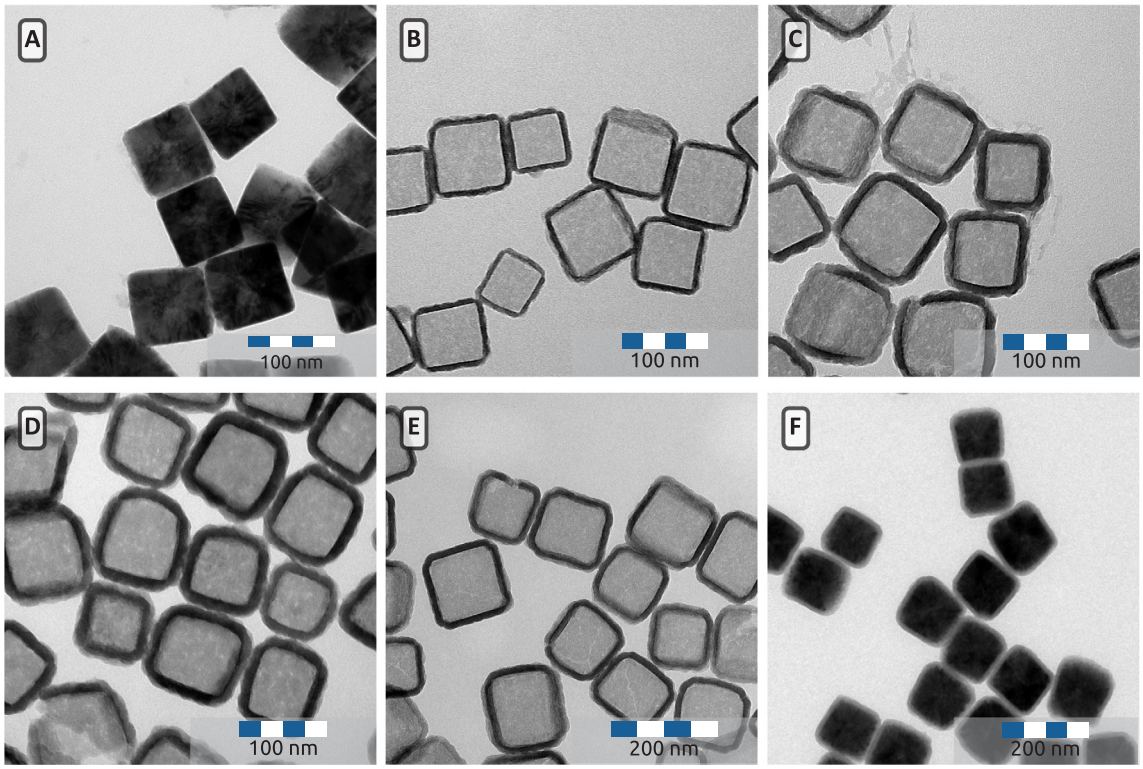

Fig. 1. TEM images of A: Cu_2O nanocubes with an average edge length of 88 ± 11 nm. B: CSS obtained from the particles depicted in A with a 5 nm thick shell; C: CSS obtained from the particles depicted in A with a 12 nm thick shell; D: CSS obtained from the particles depicted in A with a 15 nm thick shell; E: CSS with an inner void of 121 ± 20 nm and a 20 nm thick shell; F: Cu_2O core shell particles with a core of 112 ± 11 nm and a 10 nm thick shell.

Table 2
Overview of the samples measured with SAXS.

Code	Core size R_2 (nm)	Size R_1 (nm)	Concentration (mg/mL)	m value
CSS4	121 ± 20	150 ± 20	28	4.0
CCS	112 ± 11	133 ± 10	8	4.5

SI, no deviation in refractive index larger than 0.2 was observed. Therefore, we used the calculated values from Eq. (17) without further modification. The particle concentration was determined by drying a known volume and weighing the solid residue. The concentrations of the dispersions were 0.5, 0.6 and 1.8 mg/mL for CSS1, CSS2 and CSS3 respectively.

3.5. SAXS measurements

SAXS measurements were performed at the DUBBLE beamline BM-26B at the European Synchrotron Radiation Facility in Grenoble, France [53]. Scattering of X-rays with the wavelength of 1.04 Å is recorded by a Pilatus 1 M (Dectris) detector located 4.65 metres behind the sample. An evacuated fly-pass tube is inserted between sample and detector to reduce scattering of the X-ray beam in air. Intensity of the transmitted direct beam is measured by a photodiode inside a beamstop located at the end of the fly-pass tube. SiO_2@Cu_2O cubic core shell and cubic silica shells were dispersed in ethanol. The dispersions were centrifuged for 1 min at 1000 g to remove dust and clusters from the dispersion. The solid content of the dispersions was 0.8 wt % for CCS particles and 2.8 wt% for the CSS particles, as listed in Table 2.

4. Results

4.1. Form factor from SAXS

In Figs. 2 and 3, SAXS scattering curves of CSS and CCS cuboids are depicted. The scattering curve of the cubic SiO_2 shells shows three distinct intensity minima. The minima at $K = 0.0425\ nm^{-1}$ and $K = 0.0862\ nm^{-1}$, are the first and second minima from the shape of the CSS. These minima then dampen, due to the size polydispersity of the particles (13 %). At high K-values, additional oscillations become visible at $K = 0.51\ nm^{-1}$, which correspond to a length of 13 nm. These oscillations agree with an average shell thickness of 14 ± 1.1 nm as determined from TEM. The experimental scattering curve was compared to numerical models of perfect cubic shells and spherical shells, both with an edge length or radius of 150 nm and an inner void of 121 nm. The SAXS data indicate that the cuboid shape is in between that of a cube and a sphere, which corresponds to superballs with an m-value of 4. Additionally, in Fig. 2 it is visible that for both models, the minima arising from the shell thickness are at slightly lower K values than for to the SAXS data ($K = 0.42\ nm^{-1}$, vs $K = 0.50\ nm^{-1}$). This discrepancy can be attributed to polydispersity in the silica shell thickness, which is not accounted for in the models. Any roughness in the silica shell is hard to distinguish via TEM and could account for an overestimation in the shell thickness.

Similarly, in Fig. 3, the scattering curve of SiO_2@Cu_2O is compared to models of a cubic and spherical core-shell particle. Similar to the scattering curves of the cubic SiO_2 shells, the first two minima are located at K values slightly lower compared to the minima in the spherical model but at slightly higher K values compared to the cubic model. The experimental data, however, deviate significantly from the models at K values higher than $0.2\ nm^{-1}$ and no minimum is visible arising from the uniform silica shell similar

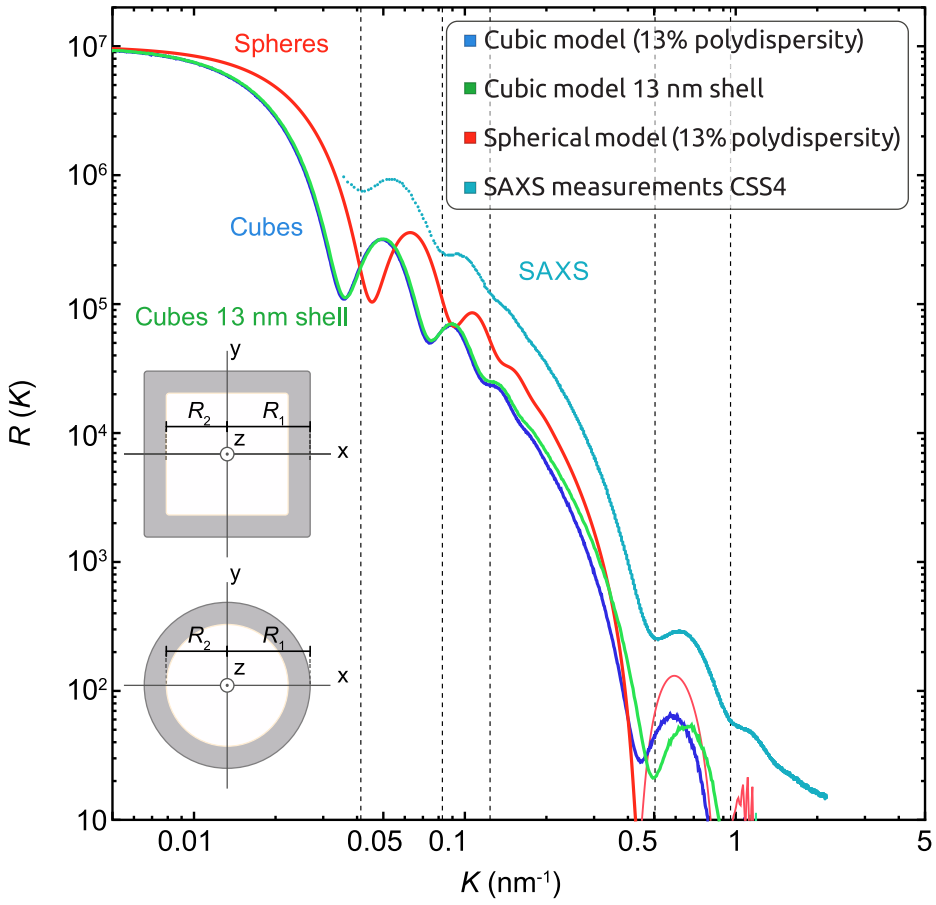

Fig. 2. Scattering curves obtained from SAXS measurements on cubic silica shells. The cyan curve is the measured scattering profile while the blue, green, and red curves are obtained from models of, respectively, a cubic 14 nm shell, a cubic 13 nm shell and a spherical 14 nm shell, all with 13% polydispersity. Inset: visual depiction of the geometric models used to calculate the form factors. (For interpretation of the references to colour in this figure legend, the reader is referred to the web version of this article.)

to the cubic silica shells. This can be explained by scattering from inhomogeneities in the cuprous-oxide core. TEM-micrographs seem to indicate that the particles are not single-crystalline, which might result in density inhomogeneities inside the Cu_2O core which cause excess scattering at high K values. These inhomogeneities within cuprous-oxide particles were earlier observed with X-ray laser diffraction [54].

4.2. Radius of gyration from the form factor

Dispersions of CSS in ethanol:DMSO (95:5, vol:vol), depicted in Fig. 1, were studied with static light scattering. Three different types of particles were prepared from the same Cu_2O cores, but coated with silica layers of varying thickness. The different cubic shells were examined to evaluate the influence of the coating thickness on the size and the effective refractive index.

To determine the size, the radius of gyration (R_g) was determined by plotting $ln(R(K))$ of the scattering intensity as a function of K^2 (Eq. (8)). In the Guinier regime ($KR_g < 3$) the data should follow linear behaviour with a slope of $-R_g^2/3$. The plots in Fig. 4 show that the obtained scattering curves indeed are linear for most scattering angles. Only in the low K-regime a small deviation from linearity behaviour is visible, probably caused by some residual dust particles or a small fraction of larger clusters. In Table 3, the measured gyration radii derived from the Guinier plots are presented and compared with values calculated from the average particle size obtained from TEM measurements (Table 1). The size obtained from SLS is in excellent agreement with the TEM data. It is known that for silica particles, the size obtained from TEM measurements is often significantly smaller than the size obtained from SLS and DLS [55]. This reduced size from TEM is caused by shrinking of the silica matrix by the electron beam [56]. Since the silica shells of our particles are thin (8–15 nm) the shrinking of the silica shell probably falls within the uncertainty of the measurements. The excellent agreement of the R_g with the TEM-data suggests that the cubes are dispersed as single particles that do not cluster.

4.3. Contrast variation

Cubic silica shells (CSS1, Fig. 1-B) were dispersed in mixtures of DMSO and ethanol. The mixtures and their corresponding refractive indices at λ = 365, 404 and 516 nm are shown in Table Figure D.1 in the SI. The obtained Guinier plots for light with λ = 365 nm are depicted in Fig. 5, showing that most curves are linear over the probed K-range. The Guinier plots for light with $[Errormml:]mathaltimg = "si143.svg" > \lambda$ = 404 nm and 516 nm are presented in the supporting information (Figure D.3 in the supporting information). In case of low contrast, as is the case for the yellow curves in Fig. 5, the intensity increases significantly at low K-values, and is probably manifesting residual dust particles, whose scattering dominates the nearly index matched CSS at low K-values.

The refractive index can be determined by plotting the square root of the zero-angle scattering intensity as function of the dispersion refractive index (see Eq. (15)). This plot should yield a straight

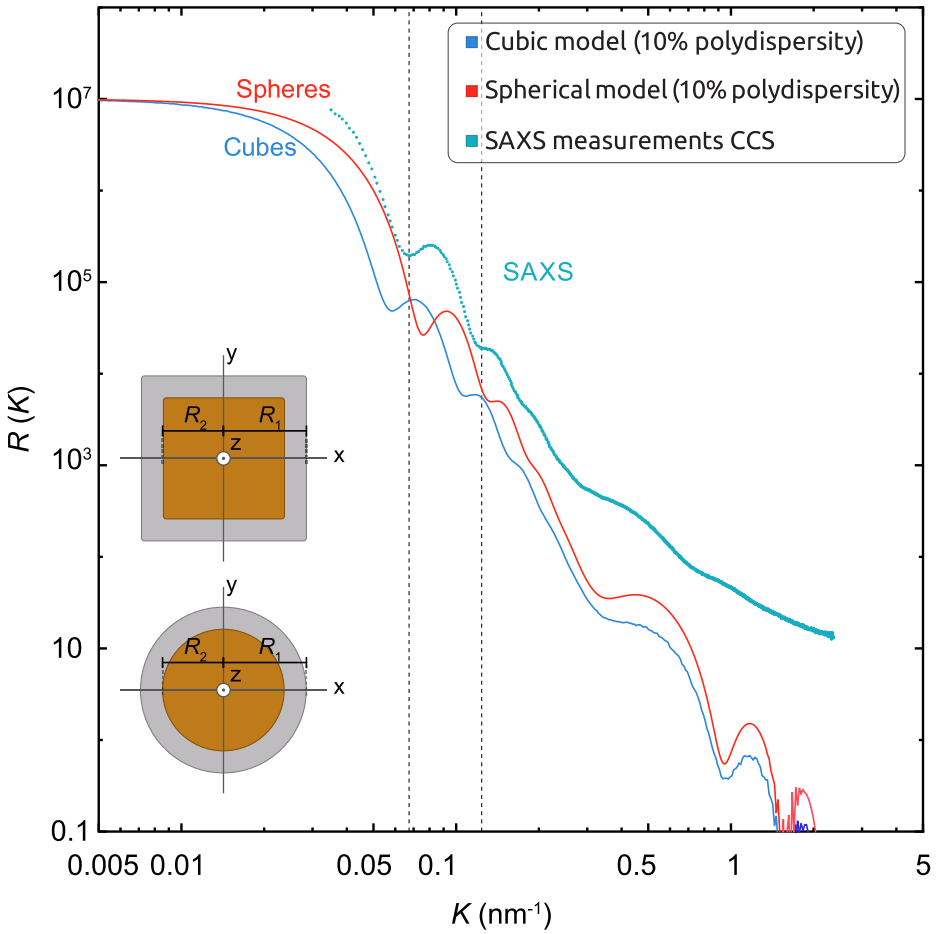

Fig. 3. Scattering curves obtained from SAXS measurements on SiO_2@Cu_2O cubic core shell particles. The cyan curve is the measured scattering profile while the blue and red curves are obtained from models of, respectively, cubic and spherical shells, both with 10% polydispersity. Inset: visual depiction of the geometric models used to calculate the form factors. (For interpretation of the references to colour in this figure legend, the reader is referred to the web version of this article.)

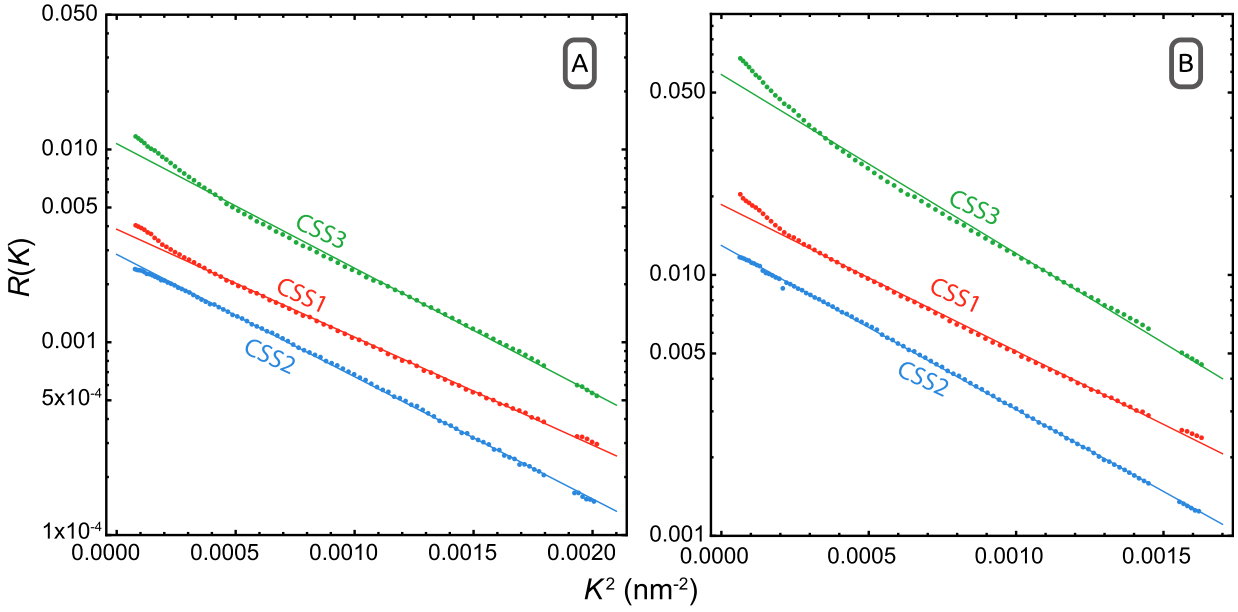

Fig. 4. Left: Guinier plots of the particles depicted in Fig. 1-B measured for light with $\lambda = 365$ nm. Right: Guinier plots of the particles depicted in Fig. 1-B measured for light with $\lambda = 404$.

Table 3
Overview of the obtained radii of gyration from SLS and TEM. [a]: standard deviation originates from the spread in particles sizes based on a number count. [b]: standard deviation originates from the standard error in first order fitting parameters of $ln(I)$ vs K^2.

Name	Core size (nm)	Size (nm)	Conc. (mg/mL)	R_g from TEM (nm)	R_g from SLS $\lambda = 365$ nm (nm)	R_g from SLS $\lambda = 404$ nm (nm)
CSS1	88 ± 9	112 ± 10	0.5	65.3 ± 6^a	66.2 ± 3^b	65.9 ± 3^b
CSS2	88 ± 9	104 ± 9	0.6	62.3 ± 6^a	62.2 ± 4^b	62.3 ± 3^b
CSS3	88 ± 9	118 ± 9	1.8	67.6 ± 7^a	66.8 ± 3^b	68.8 ± 3^b

line, where the intersection with the abscissa gives the average refractive index of the particles. In Fig. 6-A such a plot is presented for various wavelengths. From the intersects with the abscissa it follows that the particles have an average refractive index equal to 1.500, 1.494 and 1.479 for λ = 365, 404 and 516 nm, respectively.

The influence of the shell thickness on the optical properties of the particles was studied, using cubic silica shells with a shell thickness of 5 nm and 15 nm (Fig. 6-B) in contrast variation studies. The results are shown in Fig. 6-C. The average refractive index of the particles does not differ significantly from the 12 nm shell particles.

The obtained values for the average refractive index are higher than literature values for silica spheres prepared by the Stöber synthesis [49]. Two explanations for this deviation are as follows. The first explanation is the method we use to remove the cuprous oxide core. During the process, organic moieties in the silica matrix are very likely also removed, increasing the average refractive index of the particles. For conventional Stöber silica it is known that a significant amount of ethoxy groups is still present in the matrix [56], which reduces the refractive index. Another explanation could be the adsorption of DMSO in the silica pores. DMSO strongly solvates silica surfaces [57] and it is likely that DMSO preferentially adsorbs in the micropores of the silica matrix, increasing the effective refractive index of the particles. With contrast variation measurements in mixtures of DMF/DMSO, the refractive index was determined to be 1.48 ± 0.01 (Figure D.5 in the SI) for light with λ = 404 nm. The refractive index of 1.48 ± 0.01 is significantly higher compared to previously reported refractive index of unmodified Stöber silica (1.4547 ± 0.001 for λ = 436 nm), and significantly lower than the refractive index that was measured in ethanol/DMSO. The contrast variation of the silica in DMF/DMSO indicate that both the preferential adsorption of DMSO and reduced carbon content in the silica matrix influence the refractive index of the CSS.

To determine whether the refractive index of the shell is homogeneous, the intensity of different K values was evaluated and compared to the zero-angle scattering intensity. According to Eqs. 10 and 12, inhomogeneities in the refractive index of the shell lead to a different effective form factor, resulting in a different apparent refractive index with respect to the average particle refractive index. Fig. 7 shows that the intensity plots at $K = 0, 0.025$ nm^{-1} and $K = 0.04$ nm^{-1} intersect the abscissa at virtually the same value for n_s demonstrating that the shell is rather homogeneous. Moreover, the shell thickness does not seem to influence the homogeneity of the particles.

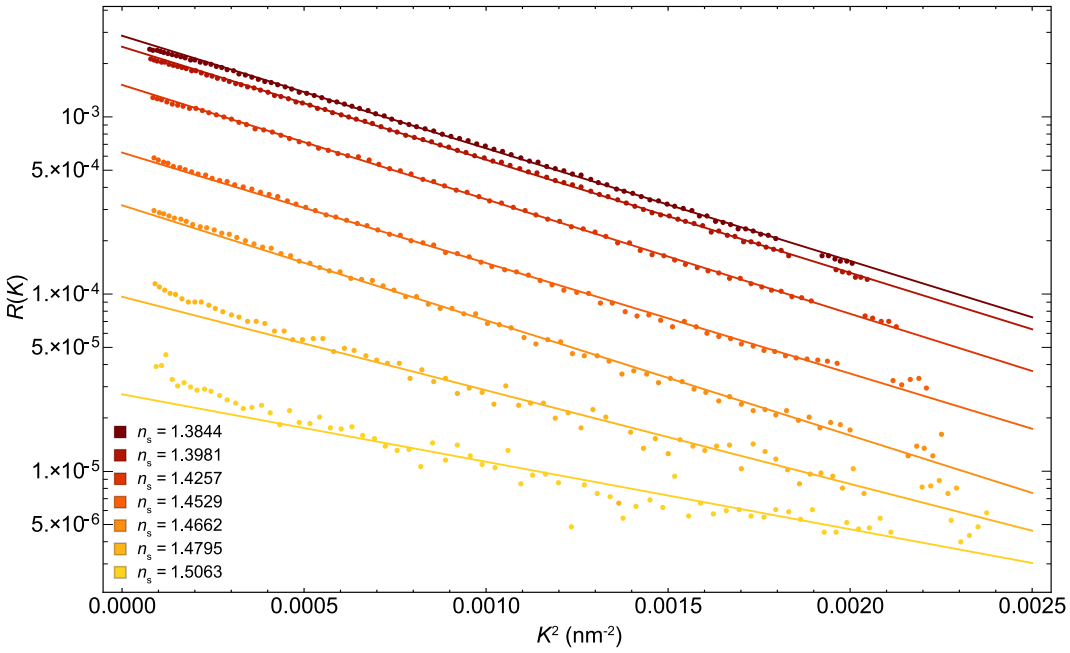

Fig. 5. Guinier plot of $R(K)$ versus K^2 obtained from sample CSS1 for light with $\lambda = 365$ nm. Symbols are measured data while the lines are a first order fit to the data points. For most curves a clear linear K^2 dependence is visible over the measured K range. For curves with the lowest contrast (yellow), the intensity data slightly deviates at low K-values. (For interpretation of the references to colour in this figure legend, the reader is referred to the web version of this article.)

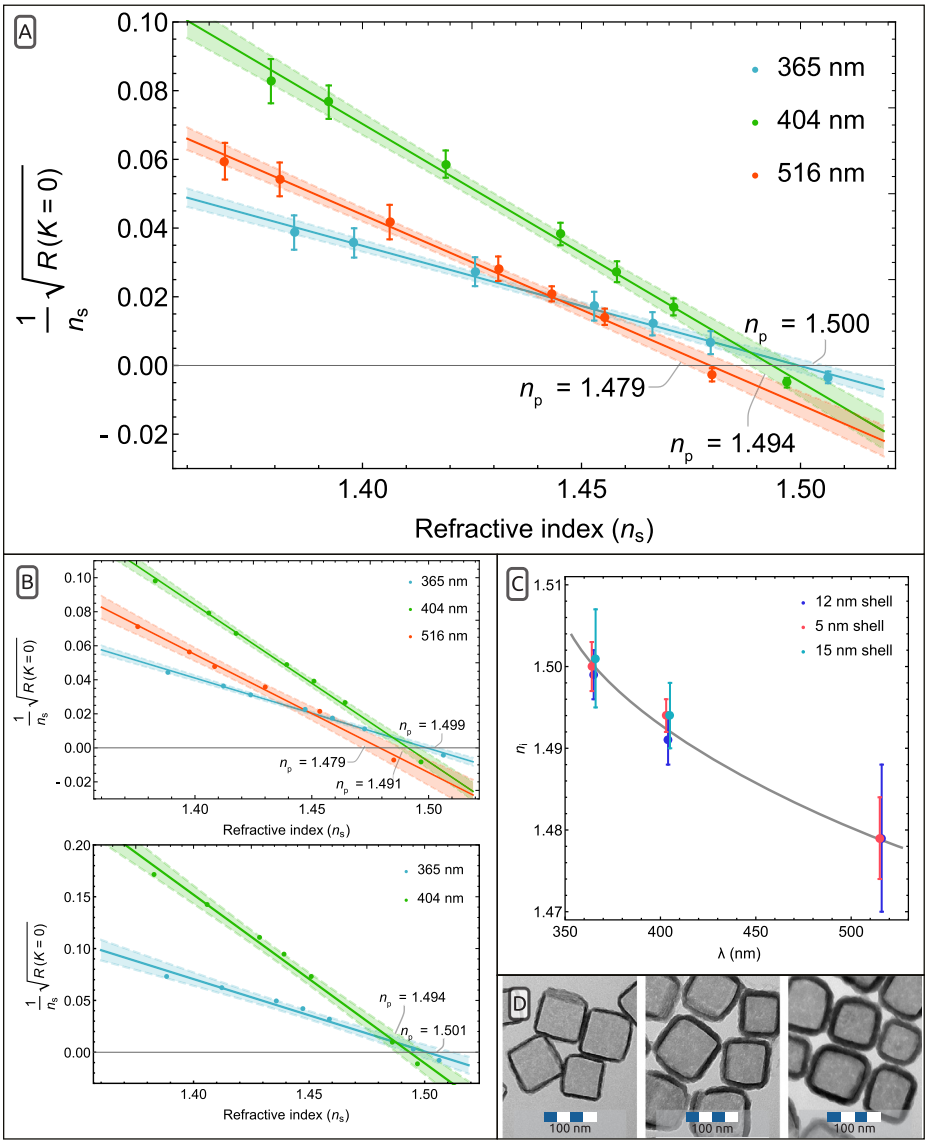

Fig. 6. A: Contrast variation experiments for CSS1 particles. The square root of the scattering intensity at $K = 0$ plotted against the refractive index of the solvent (n_s) for light with $\lambda = 365$ nm (blue), $\lambda = 404$ nm (green) and $\lambda = 516$ nm (red). The intersect with the abscissa yields the average refractive index of the particles, which is 1.500, 1.494 and 1.479 for 365, 404, and 516 nm light respectively. B: Similar as A but for CSS2 (Top) and CSS3 (Bottom) particles. C: Overview of the obtained n_p for particles with 5, 12 and 15 nm thick shell for light with $\lambda = 365$ nm, $\lambda = 404$ nm and $\lambda = 516$ nm, the line is to guide the eye. D: TEM micrographs of the CSS1 (Left), CSS2 (Middle), and CSS3 (Right) particles used in contrast variation. (For interpretation of the references to colour in this figure legend, the reader is referred to the web version of this article.)

5. Conclusions

Using both small angle X-ray scattering (SAXS) and static light scattering (SLS), we have characterised cubic silica shells derived from cuprous oxide nanocubes [5] in detail, adding to the available literature on the scattering of solid cubic particles [14,47,42,44,45] form factors of cubic core-shell particles and cubic shell particles. We find that the studied cubic silica shells form stable dispersions, suitable for detailed characterisation by different scattering techniques. From SAXS measurements, the average particle size could be obtained as well as the average shell thickness. Comparison with theoretical models, confirms that the shape of the particles is intermediate between a hollow cube and a hollow sphere. This intermediate shape is as could be expected for cubes with rounded corners which were detected earlier using TEM. SLS complements the SAXS data by providing the scattering of cubic particles at low K values. The radius of gyration of the particles from the Guinier regime corresponds well to radii of gyration calculated from TEM images using a model of cubic shells, which confirms that the particles are dispersed as single, non-aggregated particles. Contrast variation measurements show that the silica shells have a homogeneous refractive index of 1.500, 1.494 and 1.479 for light with a wavelength of 365, 404 and 516 nm, respectively. These refractive indices are significantly higher than literature values [49], which is due to both a different preparation method for the silica shell and preferential DMSO adsorption on the silica surface. The contrast variation measurements show that SLS can be used to detect small variations in the average refractive index of cubic particles resulting from solvent absorption [57] and variations in preparation methods [49].

The possibility to prepare dispersions of stable cubes with known refractive index, allows for studying the scattering of more concentrated dispersions of silica cubes, which is the subject of the accompanying paper [4]. Reducing the contrast between the solvent and the particles prevents multiple scattering and allows for the measurement of the structure factor at high concentrations.

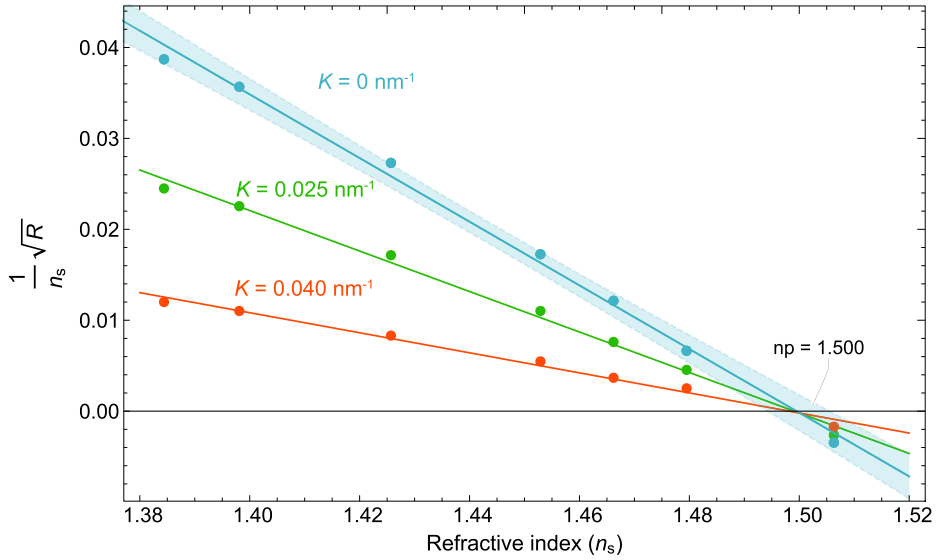

Fig. 7. The square root of the intensity versus n_s at $K = 0$ (blue), $K = 0.025$ nm^{-1} (green) and$K = 0.04$ nm^{-1} (red) for 365 nm light. The common, K-independent intersection of the different curves with the abscissa indicates the silica shell is homogeneous. (For interpretation of the references to colour in this figure legend, the reader is referred to the web version of this article.)

Further, the determined optical properties indicate the cubic silica shells are suitable for thin film anti-reflective coatings, comprising dense cube packings, which is the subject of future investigations.

Acknowledgements

This project was funded by TTW under project number 14210. Dr. Leon Bremer, Dr. Damien Reardon, Dr. Filip Oosterlinck and Dr. Jurgen Scheerder (all DSM) from the Colloidal Mosaics project User Committee are thanked for helpful discussions. NWO-TTW is acknowledged for financial support.

Appendix A. Supplementary material

Supplementary data associated with this article can be found, in the online version, at https://doi.org/10.1016/j.jcis.2019.11.002.

References

[1] T. Boublík, Equation of state of hard convex body fluids, Mol. Phys. 42 (1) (1981) 209–216, https://doi.org/10.1080/00268978100100161.
[2] R.D. Batten, F.H. Stillinger, S. Torquato, Phase behavior of colloidal superballs: shape interpolation from spheres to cubes, Phys. Rev. E 81 (6) (2010) 061105, https://doi.org/10.1103/PhysRevE.81.061105. arXiv:1005.0534.
[3] M. Marechal, U. Zimmermann, H. Löwen, Freezing of parallel hard cubes with rounded edges, J. Chem. Phys. 136 (14) (2012), https://doi.org/10.1063/1.3699086. arXiv:1202.2038.
[4] F. Dekker, B.W. Kuipers, Á. González García, R. Tuinier, A.P. Philipse, Scattering from colloidal cubic silica shells: Part II, static structure factors and osmotic equation of state, 2019, submitted for publication.
[5] F. Dekker, R. Tuinier, A. Philipse, Synthesis of hollow silica nanocubes with tuneable size and shape, suitable for light scattering studies, Colloids Interfaces 2 (4) (2018) 44, https://doi.org/10.3390/colloids2040044. http://www.mdpi.com/2504-5377/2/4/44.
[6] Y. Jiao, F.H. Stillinger, S. Torquato, Optimal packings of superdisks and the role of symmetry, Phys. Rev. Lett. 100 (24) (2008) 245504, https://doi.org/10.1103/PhysRevLett.100.245504. arXiv:0712.0420.
[7] Y. Xia, Y. Xiong, B. Lim, S.E. Skrabalak, Shape-controlled synthesis of metal nanocrystals: Simple chemistry meets complex physics?, Angew. Chem. – Int. Ed. 48 (1) (2009) 60–103, https://doi.org/10.1002/anie.200802248.
[8] K.M. Bratlie, H. Lee, K. Komvopoulos, P. Yang, G.A. Somorjai, Platinum nanoparticle shape effects on benzene hydrogenation selectivity, Nano Lett. 7 (10) (2007) 3097–3101, https://doi.org/10.1021/nl0716000.
[9] L. Gou, C.J. Murphy, Solution-phase synthesis of Cu2O nanocubes, Nano Lett. 3 (2) (2003) 231–234, https://doi.org/10.1021/nl0258776.
[10] L. Dong, Y. Chu, Y. Zhuo, W. Zhang, Two-minute synthesis of PbS nanocubes with high yield and good dispersibility at room temperature, Nanotechnology 20 (12) (2009), https://doi.org/10.1088/0957-4484/20/12/125301.
[11] D. Kim, N. Lee, M. Park, B.H. Kim, K. An, T. Hyeon, Synthesis of uniform ferrimagnetic magnetite nanocubes, J. Am. Chem. Soc. 131 (2) (2009) 454–455, https://doi.org/10.1021/ja8086906.
[12] P. Ramasamy, D.-H. Lim, B. Kim, S.-H. Lee, M.-S. Lee, J.-S. Lee, All-inorganic cesium lead halide perovskite nanocrystals for photodetector applications, Chem. Commun. 52 (10) (2016) 2067–2070, https://doi.org/10.1039/C5CC08643D. http://xlink.rsc.org/?DOI=C5CC08643D.
[13] T. Sugimoto, Y. Wang, H. Itoh, A. Muramatsu, Systematic control of size, shape and internal structure of monodisperse alpha-Fe2O3 particles, Colloids Surf., A 134 (1998) 265–279.
[14] X. Zhang, Q. Di, F. Zhu, G. Sun, H. Zhang, Wideband anti-reflective micro/nano dual-scale structures: fabrication and optical properties, Micro Nano Lett. 6 (11) (2011) 947, https://doi.org/10.1049/mnl.2011.0487.
[15] D. Wang, M. Hermes, R. Kotni, Y. Wu, N. Tasios, Y. Liu, B. De Nijs, E.B. Van Der Wee, C.B. Murray, M. Dijkstra, A. Van Blaaderen, Interplay between spherical confinement and particle shape on the self-assembly of rounded cubes, Nat. Commun. 9 (1) (2018), https://doi.org/10.1038/s41467-018-04644-4.
[16] L. Rossi, S. Sacanna, W.T.M. Irvine, P.M. Chaikin, D.J. Pine, A.P. Philipse, Cubic crystals from cubic colloids, Soft Matter 7 (9) (2011) 4139–4142, https://doi.org/10.1039/C0SM01246G. http://xlink.rsc.org/?DOI=C0SM01246G.
[17] C.D. Cwalina, K.J. Harrison, N.J. Wagner, Rheology of cubic particles in a concentrated colloidal dispersion suspending medium, AIChE J. 63 (3) (2017) 1091–1101, https://doi.org/10.1002/aic. arXiv:arXiv:1402.6991v1.
[18] C.D. Cwalina, K.J. Harrison, N.J. Wagner, Rheology of cubic particles suspended in a Newtonian fluid, Soft Matter 12 (20) (2016) 4654–4665, https://doi.org/10.1039/c6sm00205f.
[19] M. Agthe, E. Wetterskog, L. Bergström, Following the assembly of iron oxide nanocubes by video microscopy and quartz crystal microbalance with dissipation monitoring, Langmuir: ACS J. Surf. Colloids 33 (1) (2017) 303–310, https://doi.org/10.1021/acs.langmuir.6b03570.
[20] M. Agthe, K. Høydalsvik, A. Mayence, P. Karvinen, M. Liebi, L. Bergström, K. Nygård, Controlling orientational and translational order of iron oxide nanocubes by assembly in nanofluidic containers, Langmuir 31 (45) (2015) 12537–12543, https://doi.org/10.1021/acs.langmuir.5b03678.
[21] J.S. Van Der Burgt, J.J. Geuchies, B. Van Der Meer, H. Vanrompay, D. Zanaga, Y. Zhang, W. Albrecht, A.V. Petukhov, L. Filion, S. Bals, I. Swart, D. Vanmaekelbergh, Cuboidal supraparticles self-assembled from cubic CsPbBr 3 perovskite nanocrystals, J. Phys. Chem. C 122 (27) (2018) 15706–15712, https://doi.org/10.1021/acs.jpcc.8b02699.
[22] A. Tao, P. Sinsermsuksakul, P. Yang, Polyhedral silver nanocrystals with distinct scattering signatures, Angew. Chem. – Int. Ed. 45 (28) (2006) 4597–4601, https://doi.org/10.1002/anie.200601277.
[23] M.P. Boneschanscher, W.H. Evers, J.J. Geuchies, T. Altantzis, B. Goris, F.T. Rabouw, S.A. Van Rossum, H.S. Van Der Zant, L.D. Siebbeles, G. Van Tendeloo, I. Swart, J. Hilhorst, A.V. Petukhov, S. Bals, D. Vanmaekelbergh, Long-range orientation and atomic attachment of nanocrystals in 2D honeycomb superlattices, Science 344 (6190) (2014) 1377–1380, https://doi.org/10.1126/science.1252642.
[24] L.J. Sherry, S.H. Chang, G.C. Schatz, R.P. Van Duyne, B.J. Wiley, Y. Xia, Localized surface plasmon resonance spectroscopy of single silver nanocubes, Nano Lett. 5 (10) (2005) 2034–2038, https://doi.org/10.1021/nl0515753.
[25] K. Xie, P. Wu, Y. Zhou, Y. Ye, H. Wang, Y. Tang, Y. Zhou, T. Lu, Nitrogen-doped carbon-wrapped porous single-crystalline CoO nanocubes for high-performance lithium storage, ACS Appl. Mater. Interfaces 6 (13) (2014) 10602–10607, https://doi.org/10.1021/am502214k.

[26] H. Fujiwara, Spectroscopic Ellipsometry: Principles and Applications, in: Spectroscopic Ellipsometry: Principles and Applications, John Wiley & Sons, Chichester, UK, 2007, Ch. 2: Princip, pp. 13–48. arXiv:arXiv:1011.1669v3, doi: https://doi.org/10.1002/9780470060193.
[27] P.H. Lissberger, Optical applications of dielectric thin films, Rep. Prog. Phys. 33 (1) (1970) 197–268, https://doi.org/10.1088/0034-4885/33/1/305.
[28] J. Ward, Towards invisible glass, Vacuum 22 (9) (1972) 369–375.
[29] H.K. Raut, V.A. Ganesh, A.S. Nair, S. Ramakrishna, Anti-reflective coatings: a critical, in-depth review, Energy Environ. Sci. 4 (10) (2011) 3779, https://doi.org/10.1039/c1ee01297e. http://xlink.rsc.org/?DOI=c1ee01297e.
[30] P. Buskens, M. Mourad, N. Meulendijks, R. van Ee, M. Burghoorn, M. Verheijen, E. van Veldhoven, Highly porous, ultra-low refractive index coatings produced through random packing of silicated cellulose nanocrystals, Colloids Surf., A 487 (2015) 1–8, https://doi.org/10.1016/j.colsurfa.2015.09.041.
[31] A.P. Philipse, Particulate colloids: aspects of preparation and characterization, in: H. Lyklema (Ed.), Fundamentals of Interface and Colloids Science Volume IV Particulate Colloids, 1st ed., Elsevier B.V., Amsterdam, 2005, Ch. 2, pp. 2.1–2.71. doi:https://doi.org/10.1016/S1874-5679(05)80020-0.
[32] P.N. Pusey, Introduction to Scattering Experiments, in: T. Zhemb, P. Lindner (Eds.), Neutrons, X-Rays and Light. Scattering Methods Applied to Soft Condensed Matter, first ed., no. April, North Holland, 2016, Ch. 1, p. 552.
[33] A.K. Van Helden, A. Vrij, Contrast variation in light scattering: silica spheres dispersed in apolar solvent mixtures, J. Colloid Interface Sci. 76 (2) (1980) 418–433, https://doi.org/10.1016/0021-9797(80)90383-5.
[34] A. Vrij, R. Tuinier, Structure of concentrated colloidal dispersions, in: J. Lyklema (Ed.), Fundamentals of Interface and Colloids Science Volume IV Particulate Colloids, first ed., Elsevier B.V., Amsterdam, 2005, Ch. 5, p. 692. doi: https://doi.org/10.1017/CBO9781107415324.004.
[35] A. Guinier, G. Fournet, Small Angle Scattering of X-Rays, 1st Edition,., Wiley, New York, 1955, https://doi.org/10.1002/pol.1956.120199326.
[36] M. Kerker, Rayleigh-debye scattering, in: The Scattering of Light, 1969, Ch. 8, p. 688. doi:https://doi.org/10.1016/C2013-0-06195-6.
[37] J. Buitenhuis, J.K.G. Dhont, H.N.W. Lekkerkerker, Static and dynamic light scattering by concentrated colloidal suspensions of polydisperse sterically stabilized boehmite rods, Macromolecules 27 (25) (1994) 7267–7277. doi: 10.1021/ma00103a006%5Cnhttp://pubs.acs.org/doi/abs/10.1021/ma00103a006%5Cnhttp://pubs.acs.org/doi/pdf/10.1021/ma00103a006.
[38] S. Bhatia, J. Barker, A. Mourchid, Scattering of disklike particle suspensions: evidence for repulsive interactions and large length scale structure from static light scattering and ultra-small-angle neutron scattering, Langmuir 19 (3) (2003) 532–535, https://doi.org/10.1021/la0265732.
[39] A. Cao, Light scattering, Recent Appl. Anal. Lett. 36 (15) (2003) 3185–3225, https://doi.org/10.1081/AL-120026567.
[40] J.S. Pedersen, Analysis of small-angle scattering data from colloids and polymer solutions: modeling and least-squares fitting, Adv. Colloid Interface Sci. 70 (1997) 171–210, https://doi.org/10.1016/S0001-8686(97)00312-6. http://linkinghub.elsevier.com/retrieve/pii/S0001868697003126.
[41] D.H. Napper, R.H. Ottewill, Light scattering properties of cubic and octahedral particles of silver bromide, Trans. Faraday Soc. 60 (1964) 1466–1482, https://doi.org/10.1039/tf9646001466.
[42] M.R. Jones, R.J. MacFarlane, B. Lee, J. Zhang, K.L. Young, A.J. Senesi, C.A. Mirkin, DNA-nanoparticle superlattices formed from anisotropic building blocks, Nat. Mater. 9 (11) (2010) 913–917, https://doi.org/10.1038/nmat2870.
[43] S. Disch, E. Wetterskog, R.P. Hermann, A. Wiedenmann, U. Vainio, G. Salazar-Alvarez, L. Bergström, T. Brückel, Quantitative spatial magnetization distribution in iron oxide nanocubes and nanospheres by polarized small-angle neutron scattering, New J. Phys. 14 (2012), https://doi.org/10.1088/1367-2630/14/1/013025.
[44] S. Disch, E. Wetterskog, R.P. Hermann, D. Korolkov, P. Busch, P. Boesecke, O. Lyon, U. Vainio, G. Salazar-Alvarez, L. Bergström, T. Brückel, Structural diversity in iron oxide nanoparticle assemblies as directed by particle morphology and orientation, Nanoscale 5 (9) (2013) 3969–3975, https://doi.org/10.1039/c3nr33282a.
[45] J.M. Meijer, A. Pal, S. Ouhajji, H.N. Lekkerkerker, A.P. Philipse, A.V. Petukhov, Observation of solid-solid transitions in 3D crystals of colloidal superballs, Nat. Commun. 8 (2017) 14352, https://doi.org/10.1038/ncomms14352.
[46] H.J. Yang, S.Y. He, H.L. Chen, H.Y. Tuan, Monodisperse copper nanocubes: synthesis, self-assembly, and large-area dense-packed films, Chem. Mater. 26 (5) (2014) 1785–1793, https://doi.org/10.1021/cm403098d.
[47] D.H. Napper, R.H. Ottewil, Light scattering by cubic particles in the rayleigh-gans region, Kolloid-Zeitschrift und Zeitschrift für Polymere 192 (1964) 114–117.
[48] X. Li, L. Xue, Y. Han, Broadband antireflection of block copolymer/homopolymer blend films with gradient refractive index structures, J. Mater. Chem. 21 (15) (2011) 5817–5826, https://doi.org/10.1039/C0JM04508J.
[49] A.P. Philipse, C. Smits, A. Vrij, A light scattering contrast variation study on nonaqueous suspensions of coated silica spheres, J. Colloid Interface Sci. 129 (2) (1989) 335–352, https://doi.org/10.1016/0021-9797(89)90447-5.
[50] C. Graf, D.L. Vossen, A. Imhof, A. Van Blaaderen, A general method to coat colloidal particles with silica, Langmuir 19 (17) (2003) 6693–6700, https://doi.org/10.1021/la0347859. arXiv:/link.springer.com/article/10.1023%2FA%3A1025520116015.
[51] S.I. Castillo, S. Ouhajji, S. Fokker, B.H. Erné, C.T. Schneijdenberg, D.M. Thies-Weesie, A.P. Philipse, Silica cubes with tunable coating thickness and porosity: from hematite filled silica boxes to hollow silica bubbles, Microporous Mesoporous Mater. 195 (2014) 75–86, https://doi.org/10.1016/j.micromeso.2014.03.047. http://linkinghub.elsevier.com/retrieve/pii/S1387181114001942.
[52] V.A. Markel, Introduction to the Maxwell Garnett approximation: tutorial, J. Opt. Soc. Am. A 33 (7) (2016) 1244, https://doi.org/10.1364/JOSAA.33.001244. https://www.osapublishing.org/abstract.cfm?URI=josaa-33-7-1244.
[53] W. Bras, I.P. Dolbnya, D. Detollenaere, R. Van Tol, M. Malfois, G.N. Greaves, A.J. Ryan, E. Heeley, Recent experiments on a combined small-angle/wide-angle X-ray scattering beam line at the ESRF, J. Appl. Crystallogr. 36 (3 I) (2003) 791–794, https://doi.org/10.1107/S002188980300400X.
[54] T. Oroguchi, T. Yoshidome, T. Yamamoto, M. Nakasako, Growth of cuprous oxide particles in liquid-phase synthesis investigated by X-ray laser diffraction, Nano Lett. 18 (8) (2018) 5192–5197, https://doi.org/10.1021/acs.nanolett.8b02153.
[55] A.P. Philipse, A. Vrij, Polydispersity probed by light scattering of secondary particles in controlled growth experiments of silica spheres, J. Chem. Phys. 87 (10) (1987) 5634, https://doi.org/10.1063/1.453536.
[56] A.K. Van Helden, J.W. Jansen, A. Vrij, Preparation and characterization of spherical monodisperse silica dispersions in nonaqueous solvents, J. Colloid Interface Sci. 81 (2) (1981) 354–368, https://doi.org/10.1016/0021-9797(81)90417-3.
[57] G.H. Koenderink, M.P. Lettinga, A.P. Philipse, Rotational dynamics of charged colloidal spheres: role of particle interactions, J. Chem. Phys. 117 (16) (2002) 7751–7764, https://doi.org/10.1063/1.1509054. http://aip.scitation.org/doi/10.1063/1.1509054.